Springer

KSME

Journal of Mechanical Science and Technology 32 (7) (2018) 2987~2998
www.springerlink.com/content/1738-494x(Print)/1976-3824(Online)
DOI 10.1007/s12206-018-0602-1

Dynamic modeling and simulation of EMS Maglev vehicle to evaluate the levitation stability and operational safety over an elastic segmented switch track †

Jong-Boo Han[1], Hyung-Suk Han[2], Jong-Min Lee[2,*] and Sung-Soo Kim[3]

[1]*Graduate School of Mechanical Design and Mechatronics Engineering, Chungnam National University, Daejeon 305-764, Korea*
[2]*Department of Magnetic Levitation and Linear Drive, Korea Institute of Machinery and Materials, Daejeon 305-343, Korea*
[3]*Department of Mechatronics Engineering, Chungnam National University, Daejeon 305-764, Korea*

(Manuscript Received April 3, 2016; Revised April 21, 2017; Accepted March 23, 2018)

Abstract

An electromagnetic suspension (EMS) magnetic levitation (Maglev) vehicle runs between a guideway and electromagnet at a certain distance, usually called the "airgap". To maintain the vertical airgap, the electric current of the electromagnet must be controlled. A lateral restoring force is generated by a component force in the vertical direction but is not controlled. So, the EMS Maglev vehicle must be operated at appropriate speeds around curves to prevent contact with the track. This is particularly important at track sections with a small radius of curvature such as at a switch. The segmented switch system developed and employed in Korea is entirely made of steel, which may cause instabilities in the levitation system in the presence of an airgap due to its greater susceptibility to vibration compared to concrete. Therefore, it is necessary to evaluate the stability of levitation using computational simulation when the maglev vehicle ran over a segmented switch. In this paper, a dynamic model of a Maglev vehicle was developed based on multibody dynamics that accounts for the flexibility of the segmented switch track. Using the developed analytical model, levitation stability and operational safety simulations were carried out.

Keywords: EMS Maglev vehicle; Segmented switch; Airgap; Dynamics modeling and simulation

1. Introduction

Magnetic levitation (Maglev) vehicles have been developed in Germany, Japan, the United States, Korea, and China since the 1970s as a safer and more efficient transportation system. In particular, the Maglev vehicle expected to be deployed in Incheon, Korea, was designed to have a top speed of 110 km/h and to be operated in urban areas. A Maglev vehicle runs by maintaining a certain distance between the guideway and electromagnet to prevent dust infiltration and noise generation. However, the Maglev vehicle always runs above the elevated guideway. Therefore, the levitation stability must be evaluated to ensure reliability regardless of the dynamic characteristics of the guideway. Many analytical and experimental Maglev vehicle stability studies have been performed in Korea [1-6] but few studies have been devoted to the evaluation of levitation stability and running safety on a switch track.

There are two types of switch: the bending switch and the segmented switch. As shown in Fig. 1(a), the bending switch structure is long, has a large radius of curvature, and is designed for high-speed passes. In contrast, the segmented switch is short, can only be used at low speed, and is designed for use on a narrow path in an urban area (Fig. 1(b)). Since the proposed Maglev vehicle is to be operated at low speeds in an urban area, the segmented-type switch was adopted and developed [7, 8].

(a) Bending switch (b) Segmented switch

Fig. 1. Flow chart for the correction of the roll forming process design.

The Korean segmented switch has an angle-relieving device between segments that creates a 2.3° curve at every segment as shown in Fig. 2. A knee point is generated by the segment, leading to a discontinuous curve. Therefore, if the lateral restoring force of the electromagnet is not sufficient at excessive speeds, the vehicle can make contact with the switch track. The contact of the magnetic levitation system can be ex-

*Corresponding author. Tel.: +82 42 868 7199, Fax.: +82 42 868 7618
E-mail address: lee_jm@kimm.re.kr
† Recommended by Associate Editor Hyoun Jin Kim

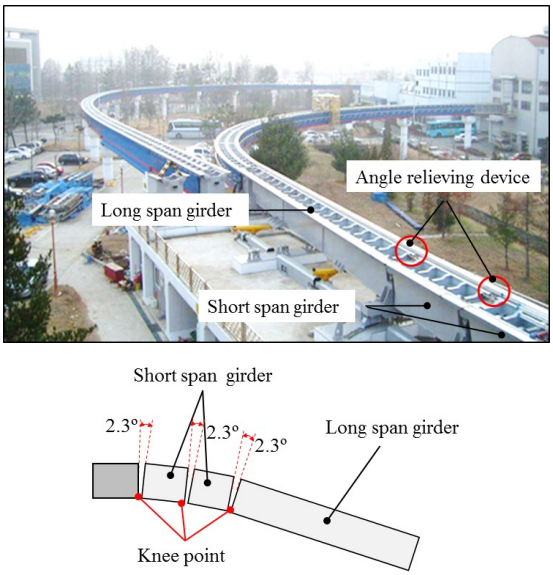

Fig. 2. Discontinuity of the curve in the segmented switch.

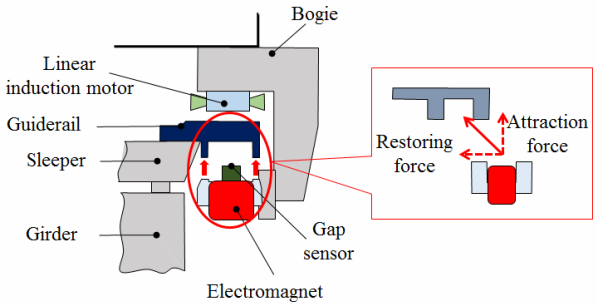

Fig. 3. Principle of levitation in EMS Maglev vehicles.

pressed as failure of levitation. In addition, the segmented switch is entirely made of steel and is therefore more susceptible to vibrations than concrete [9].

These characteristics of the segmented switch present a serious weakness in the design of Maglev vehicles that use a U-shaped electromagnet. The magnetic levitation method of the U-shaped electromagnet suspension (EMS) is inherently unstable [10]. As shown in Fig. 3, the principle of levitation of an electromagnetic levitation vehicle is to send actively-controlled electrical currents in the electromagnetic coil to generate an attraction force in the airgap between the electromagnet core of the U-shaped structure and a guiderail. When the electromagnet's core is dislocated from the facing side of the guiderail as shown in Fig. 3, a restoring force is generated passively in the lateral direction [10]. Therefore, as the vehicle operates without contact between bogie and guiderail over a curved switch track, their top operational speed must be evaluated. Also, it must be evaluated whether their vertical airgap could be kept or not in the structural vibrations of switch track made of steel.

The evaluation of the stability and safety of a Maglev vehicle under actual operating conditions involves significant in-

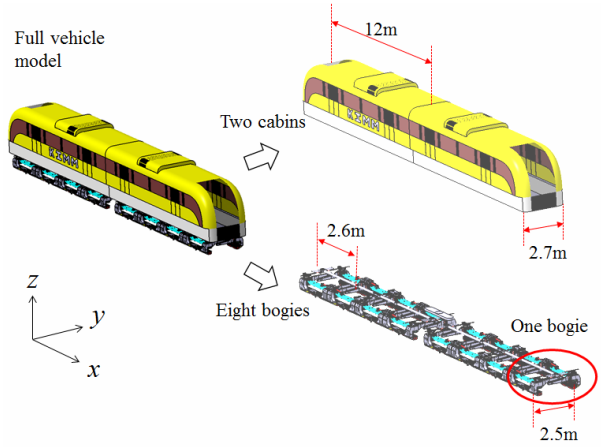

(a) Full dynamics model of Maglev

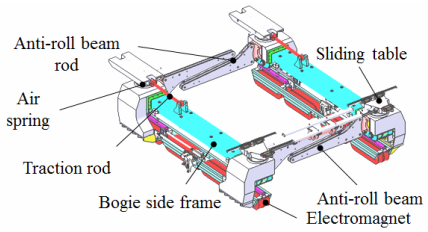

(b) Configuration of each bogie

Fig. 4. Full Maglev vehicle.

vestments of capital and time along with the risk of accidents. Therefore, in this paper, a multibody dynamics model of a Maglev vehicle was developed based on virtual prototyping to perform an analysis of the safety and stability of the model in conditions similar to actual operating conditions.

2. Integrated model of a Maglev vehicle based on multibody dynamics

In this section, the modeling of each subsystem of the Maglev vehicle is described. The vehicle consists of a cabin, a bogie system, and an air spring that plays the role of a secondary suspension. The vehicle was considered to be rigid. Virtual. Lab Motion [11], a multibody dynamics analysis program, was used to develop the model. The electromagnetic force and the levitation controller were developed as a user-defined function consisting of an ordinary differential equation that could be called to match a given situation. In addition, the vibration modes were analyzed using the ANSYS software package to take flexibility into account. The segmented switch was modeled using the mode superposition method by selecting the appropriate vibration mode. The detailed modeling process is discussed in each of the following subsections.

2.1 Modeling the Maglev vehicle

Fig. 4 shows a Maglev vehicle that consists of two cabins and eight bogies. The cabin is 12 m long and 2.7 m wide. The bogie is 2.6 m long and 2.5 m wide. An air spring serves as a

Table 1. Specifications of joint and force elements.

Elements	Type	Body	
		i-th	j-th
Joint	Bracket joint	Electromagnet	Bogie side frame
	Revolute joint	Traction rod	Sliding table
	Revolute joint	Traction rod	Bogie side frame
	Translational joint	Sliding table	Cabin
	Distance constraint	Anti-roll beam	Anti-roll beam
Force	Bushing	Anti-roll beam	Bogie side frame
	Bushing	Sliding table	Bogie side frame

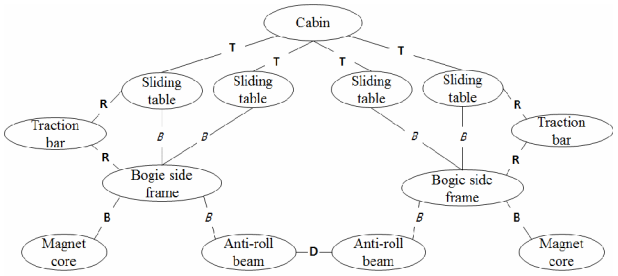

Fig. 5. System topology of a bogie on a Maglev vehicle.

secondary suspension mechanism and is located at each corner between the cabin and the bogie. Sliding tables restrict motion in the lateral direction when running through a curve and are located at the front and rear of the bogie. Anti-roll beams are placed at the front and rear of the bogie to prevent rolling and separate the right and left frames of the bogie. In addition, a rod is installed between the anti-roll beams. A traction rod connects the bogie and the sliding table, which makes it possible for the vehicle to move with the bogie. Finally, a total of eight electromagnets are attached on the right and left sides (four pairs on each side) in order to levitate the Maglev vehicle.

Kinematic modeling was used to ensure proper connections between the components of the bogie. Fig. 5 is the system topology of the bogie (Fig. 4(b)) and shows the kinematic constraints applied to each body. A bushing element was used to minimize the number of parts and joints and to eliminate redundancy. The rod that connects the anti-roll beams is considered to be a massless link and used as the distance constraint. Table 1 lists the force elements and the joint relationships of each body. Table 2 covers the dynamic properties of the cabin, bogie, and electromagnets. Table 3 shows the specifically model data of air spring as a secondary suspension.

Using multibody dynamics, the bogie was modeled in differential algebraic equation (DAE) form as described in Eq. (1) in Cartesian coordinates. $\mathbf{M}$ is the mass and inertia matrix of each object, $\mathbf{Q}$ is the force vector acting on each object, $\mathbf{\Phi}_{\mathbf{y}}$ is the Jacobian matrix of the constraint conditions for each object, $\ddot{\mathbf{y}}$ is the acceleration vector of each object,

Table 2. Inertia properties of the Maglev vehicle.

Inertia properties	Mass (kg)	Inertia (kg·m^2)		
		Ixx	*Iyy*	*Izz*
Cabin	1.8×10^4	3.1×10^5	2.2×10^5	2.2×10^5
Bogie side frame	6.6×10^2	5.4×10^1	7.1×10^2	6.7×10^2
Electromagnet	1.3×10^2	2.1×10^{-1}	2.3×10^1	2.3×10^1
Sliding table	1.1×10^1	1.0×10^{-1}	1.3×10^{-1}	2.2×10^{-1}
Traction rod	1.1×10^1	5.2×10^{-4}	5.0×10^{-2}	5.0×10^{-2}
Anti-roll beam	4.2	4.4×10-1	2.0×10-2	4.2×10-1
Anti-roll beam rod	9.0×10-2	4.4×10-4	4.4×10-4	8.6×10-6

Table 3. Specification of air spring.

Items	Specification	
Air spring stiffness (N/m)	Vertical	62000
	Lateral	140000
Air spring damping (kg/s)	Vertical	1600
	Lateral	1300

$\boldsymbol{\lambda}$ is the Lagrange multiplier vector, and $\boldsymbol{\gamma}$ is the acceleration vector of the constraint condition [12]. In addition, $\bar{\mathbf{Q}}$ is represented as a general gravitational force, $\bar{F}$ is the reaction force of each body connected with the bushing element, and F_{em} is the electromagnet force used to control the airgap [13].

$$\begin{bmatrix} \breve{\mathbf{M}}_{bogie} & \mathbf{\Phi}_{\ddot{\mathbf{y}}}^{T} \\ \mathbf{\Phi}_{\ddot{\mathbf{y}}} & \mathbf{0} \end{bmatrix} \begin{bmatrix} \ddot{\breve{\mathbf{y}}}_{bogie} \\ \breve{\boldsymbol{\lambda}} \end{bmatrix} = \begin{bmatrix} \breve{\mathbf{Q}}_{bogie} \\ \breve{\boldsymbol{\gamma}} \end{bmatrix} \tag{1}$$

where

$$\breve{\mathbf{M}}_{bogie} = \begin{bmatrix} \bar{\mathbf{M}}_{b.f} & & & \\ & \bar{\mathbf{M}}_{em} & & synn \\ & & \bar{\mathbf{M}}_{s.t} & \\ & \mathbf{0} & & \bar{\mathbf{M}}_{t.r} \\ & & & & \bar{\mathbf{M}}_{a.b} \end{bmatrix},$$

$$\ddot{\breve{\mathbf{y}}}_{bogie} = \begin{bmatrix} \ddot{\bar{\mathbf{y}}}_{b.f} \\ \ddot{\bar{\mathbf{y}}}_{em} \\ \ddot{\bar{\mathbf{y}}}_{s.t} \\ \ddot{\bar{\mathbf{y}}}_{t.r} \\ \ddot{\bar{\mathbf{y}}}_{a.b} \end{bmatrix}, \quad \breve{\mathbf{Q}}_{bogie} = \begin{bmatrix} \bar{\mathbf{Q}}_{b.f} - \bar{F}_{a.b} - \bar{F}_{a.s} \\ \bar{\mathbf{Q}}_{em} - \bar{F}_{em} \\ \bar{\mathbf{Q}}_{s.t} - \bar{F}_{a.s} \\ \bar{\mathbf{Q}}_{t.r} \\ \bar{\mathbf{Q}}_{a.b} - \bar{F}_{a.b} \end{bmatrix}$$

b.f: Bogie side frame, *em*: Electromagnet, *s.t*: Sliding table, *t.r*: Traction rod, *a.b*: Anti-roll beam, *a.s*: Air spring.

If the equation of motion shown in Eq. (1) is applied to the entire vehicle model, the full equation of motion can be expressed as Eq. (2). The bogie has 31 degrees of freedom and the full vehicle model has approximately 240 degrees of freedom.

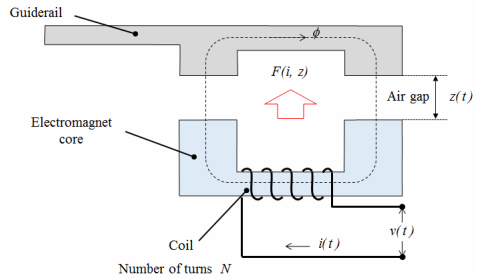

Fig. 6. Schematic of an electromagnet.

$$\begin{bmatrix} \mathbf{M} & \mathbf{\Phi}_{\mathrm{y}}^{T} \\ \mathbf{\Phi}_{\mathrm{y}} & \mathbf{0} \end{bmatrix} \begin{bmatrix} \ddot{\mathbf{y}} \\ \boldsymbol{\lambda} \end{bmatrix} = \begin{bmatrix} \mathbf{Q} \\ \boldsymbol{\gamma} \end{bmatrix} \tag{2}$$

where

$$\mathbf{M} = \begin{bmatrix} \mathbf{M}_{cabin} & & & synn \\ & \breve{\mathbf{M}}_{bogie1} & & \\ & & \ddots & \\ \mathbf{0} & & & \breve{\mathbf{M}}_{bogie8} \end{bmatrix},$$

$$\ddot{\mathbf{y}} = \begin{bmatrix} \ddot{\mathbf{y}}_{cabin} \\ \breve{\ddot{\mathbf{y}}}_{bogie1} \\ \vdots \\ \breve{\ddot{\mathbf{y}}}_{bogie8} \end{bmatrix}, \mathbf{Q} = \begin{bmatrix} \mathbf{Q}_{cabin} \\ \breve{\mathbf{Q}}_{bogie1} \\ \vdots \\ \breve{\mathbf{Q}}_{bogie8} \end{bmatrix}.$$

2.2 Modeling the electromagnet

In general, the electromagnet consists of a coil wound around a core as shown in Fig. 6. When an electrical current is supplied through the coil, a magnetic field is formed with a flux density (B). An attraction force is generated in the airgap (z) that is dependent on the electrical current (i) in the vertical direction:

$$F_{em}(\mathrm{i}, \mathrm{z}) = \frac{B^2 A}{\mu_0} = \frac{\mu_0 N^2 A}{4}\left(\frac{i(t)}{z(t)}\right)^2 \tag{3}$$

where A is the sectional area of the core and μ_0 is the permeability of the air [14].

The electrical current in Eq. (3) can be expressed as a function of the source and inductance of the coil using Kirchhoff's voltage law:

$$v(t) = Ri(t) + \frac{d}{dt}\left(L(z, i)\cdot i(t)\right) \tag{4}$$

where R is resistance of the circuit and L is the inductance. L is inversely proportional to the electrical current and directly proportional to magnetic flux. The magnetic flux is dependent on the resistance of the airgap:

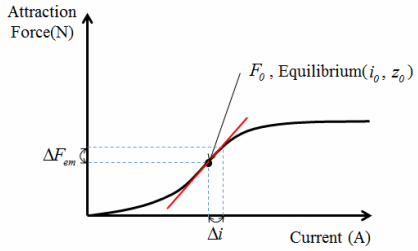

Fig. 7. Linearization of attraction force about the equilibrium point.

$$L(\mathrm{z}, \mathrm{i}) = \frac{N}{i}\phi = \frac{N}{i(t)}\frac{Ni(t)}{R_T} = \frac{N^2}{R_T} \tag{5}$$

where R_T is the reluctance and is defined as $R_T = l / \mu_0 A$. Using the equation $l = 2z(\mathrm{t})$, Eq. (5) may be rewritten to give

$$L(\mathrm{z}, \mathrm{i}) = \frac{\mu_0 N^2 A}{2z(t)}. \tag{6}$$

Therefore, the voltage in Eq. (4) can be finally expressed as

$$v(t) = Ri(t) + \frac{\mu_0 N^2 A}{2}\frac{d}{dt}\left(\frac{i(t)}{z(t)}\right). \tag{7}$$

In general, the electromagnetic force has non-linear characteristics. It becomes saturated at a certain level even though the electric current may increase. In this study, to efficiently control the electromagnetic force, the electromagnet model was linearized since there were no significant differences between the linear and non-linear electromagnet model within the specified control range [15]. Therefore, it was assumed that the attraction force increases linearly about the equilibrium point (i_0 , z_0) to support a Maglev vehicle as shown in Fig. 7. Eqs. (3) and (4) can be expanded in a Taylor series up to the second term to give linearized equations [14]:

$$F_{em}(\mathrm{i}, \mathrm{z}) = F_0 + \Delta F_{em} = F_0 + (-K_i \Delta i + K_z \Delta z) \tag{8}$$

$$v(t) = v_0 + L_0 \Delta \dot{i} - K_i \Delta \dot{z} \tag{9}$$

where

$$F_0 = \frac{\mu_0 N^2 A}{4}\left(\frac{i_0}{z_0}\right)^2, v_0 = Ri_0, L_0 = \frac{\mu_0 N^2 A}{2}\left(\frac{1}{z_0^2}\right),$$

$$K_i = \frac{\mu_0 N^2 A}{2}\left(\frac{i_0}{z_0^2}\right), K_z = \frac{\mu_0 N^2 A}{2}\left(\frac{i_0^2}{z_0^3}\right).$$

The electromagnetic force in Eq. (8) can be divided into a vertical attraction force F_{att} expressed by Eq. (10) and a lateral restoring force F_{res} expressed by Eq. (11). When the lateral airgap Δy is equal to zero, the lateral restoring force becomes zero.

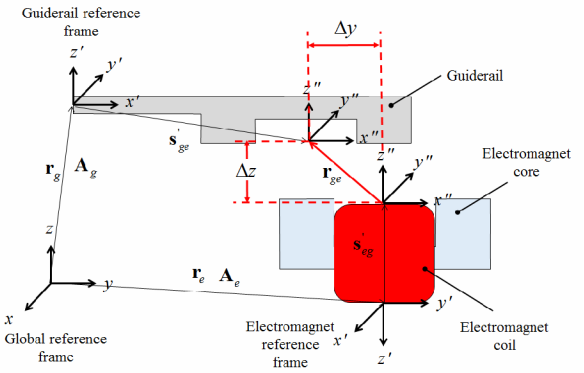

Fig. 8. Definition of vectors for calculation of the airgap.

$$F_{att} = F_{em}\left(1+\frac{2\Delta z}{\pi\omega_m}+\frac{2\Delta y}{\pi\omega_m}\tan^{-1}\left(\frac{\Delta z}{\Delta y}\right)\right) \tag{10}$$

$$F_{res} = F_{em}\left(-\frac{2\Delta z}{\pi\omega_m}\tan^{-1}\left(\frac{\Delta y}{\Delta z}\right)\right). \tag{11}$$

2.3 Modeling the electromagnet controller

In the Maglev vehicle, the airgap is the distance between the guideway and electromagnet. The coordinate systems used for the guiderail and electromagnet are defined as shown in Fig. 8. $\mathbf{r}_g$ and $\mathbf{r}_e$ are the vectors from the global coordinate system to the guiderail and electromagnet coordinate systems, respectively. $\mathbf{A}_g$ and $\mathbf{A}_e$ are coordinate transformation matrices. $\mathbf{r}_{ge}$ is the airgap vector, expressing the vertical and lateral airgaps as Δz and Δy, respectively. The airgap vector $\mathbf{r}_{ge}$ can be calculated using Eq. (12). The differential values of the airgap vector can be obtained by differentiation with respect to time [1], expressed in Eq. (13).

$$\mathbf{r}_{ge} = \mathbf{r}_g + \mathbf{A}_g\mathbf{s}'_{ge} - (\mathbf{r}_e + \mathbf{A}_e\mathbf{s}'_{eg}) \tag{12}$$

$$\dot{\mathbf{r}}_{ge} = \dot{\mathbf{r}}_g + \mathbf{A}_g\tilde{\boldsymbol{\omega}}'_g\mathbf{s}'_{ge} - (\dot{\mathbf{r}}_e + \mathbf{A}_e\tilde{\boldsymbol{\omega}}'_e\mathbf{s}'_{eg}). \tag{13}$$

To obtain Δi, Eq. (9) is solved for $\Delta\dot{i}$ and expressed as Eq. (14). If $v(t)$ is known, it is possible to get $\Delta\dot{i}$. $v(t)$ is the magnitude of control voltage needed to correct perturbations in the airgap for airgap control of a Maglev vehicle.

$$\Delta\dot{i} = \frac{1}{L_0}v(t) + \frac{K_i}{L_0}\Delta\dot{z} - \frac{v_0}{L_0}. \tag{14}$$

The proportional integral differential (PD) method is used as the electromagnet control method for the Maglev vehicle. The levitation airgap between the guideway and electromagnet in an actual system $\mathbf{r}_{ge}(z)$ is received by a gap sensor. In addition, the acceleration of the electromagnet $\ddot{\mathbf{r}}_e(z)$ is measured in the vertical direction using an acceleration sensor. Five states are estimated through an observer by entering the two values obtained above into Eq. (13). The observer used for electromagnet control restores the hidden low frequencies

Table 4. Parameters of electromagnet, control gain, and observer.

Electromagnet		Control gain		Observer	
Items	values	Items	values	Items	values
μ_0 (H·m^{-1})	4π x 10^{-7}	K_{zpp}	4	T_1	0.2
N	396	K_{zp}	40	T_2	0.01
A (m2)	0.038	K_z	7	T_3	0.3127
i_0 (A)	24	K_{gp}	40	T_4	0.00022
z_0 (m)	0.08	K_g	7	T_5	0.02
				V_1	1.3
-				V_2	1.0
				V_3	0.2

by using the measured gap signal and a high pass filter for the acceleration measurements. The reason for using this method is that the low frequency accelerations may be turned into noise due to the deflection of the guideway and the changes in gravitational acceleration caused by the slope of the curve itself. $T_1 - T_5$ in Eq. (16) refer to time constants that determine the cut-off frequency of the high pass and low pass filters and $V_1 - V_3$ define the damping ratios of each filter. Using the output $\mathbf{y}$ obtained here, the voltage is calculated using Eq. (16). Table 4 lists the parameters related to the electromagnet controller and the electromagnet used in the actual analysis [2]. And, also the estability of state-feedback controller with the Eq. (15) had been done in Ref. [14].

$$\begin{aligned}\dot{\mathbf{x}} &= \mathbf{A}_c\mathbf{x} + \mathbf{B}_c\mathbf{u}\\ \mathbf{y} &= \mathbf{C}_c\mathbf{x} + \mathbf{D}_c\mathbf{u}\end{aligned} \tag{15}$$

where

$$\mathbf{y} = \left[\Delta\ddot{\hat{z}} \quad \Delta\dot{\hat{z}} \quad \Delta\hat{z} \quad \Delta\dot{\hat{g}} \quad \Delta\hat{g}\right]^T,$$

$$\mathbf{u} = \left[\ddot{\mathbf{r}}_e(z) \quad \mathbf{r}_{ge}(z)\right]^T$$

$$\mathbf{A}_c = \begin{bmatrix} 0 & \frac{1}{T_3} & 0 & -\frac{1}{T_3} & 0 \\ -\frac{1}{T_1} & -\frac{V_1}{T_1} & 0 & \frac{V_1}{T_1} & 0 \\ 0 & \frac{1}{T_2} & -\frac{V_2}{T_2} & 0 & \frac{V_2}{T_2} \\ 0 & 0 & 0 & -\frac{V_3}{T_4} & -\frac{1}{T_4} \\ 0 & 0 & 0 & -\frac{1}{T_5} & 0 \end{bmatrix}, \quad \mathbf{B}_c = \begin{bmatrix} 0 & 0 \\ \frac{1}{T_1} & 0 \\ 0 & 0 \\ 0 & \frac{1}{T_4} \\ 0 & 0 \end{bmatrix},$$

$$\mathbf{C}_c = \begin{bmatrix} -1 & -V_1 & 0 & V_1 & 0 \\ 0 & 1 & 0 & 0 & 0 \\ 0 & 0 & 1 & 0 & 0 \\ 0 & 0 & 0 & 1 & 0 \\ 0 & 0 & 0 & 0 & 1 \end{bmatrix}, \quad \mathbf{D}_c = \begin{bmatrix} 1 & 0 \\ 0 & 0 \\ 0 & 0 \\ 0 & 0 \\ 0 & 0 \end{bmatrix}. \tag{16}$$

Using the control voltage obtained from Eq. (16) the differential value of electric current $\Delta\dot{i}$ in Eq. (14) was estimated. Δi was then calculated by integrating the first order ordinary differential equation function. Hence, all the unknown values in Eq. (8) can be calculated and the controllable electromagnetic force ΔF_{em} can also be calculated. The electromagnet and the electromagnet controller shown in Secs. 2.2 and 2.3 are implemented via a user subroutine.

2.4 Modeling the flexibility of the segmented switch

To take the flexibility of the segmented switch into account, the vibration modes of the structure were analyzed. The mode superposition method was used by selecting a major mode. We made the assumption that the structure is a secondary spring-damper system. The governing equations of the forced vibration can be expressed as in Eq. (17). Mapping to modal coordinates gives Eq. (18) where $\boldsymbol{\Psi}$ is the mode shape matrix that consists of selected vibration modes and α is a modal coordinate vector.

$$\mathbf{M}\ddot{x} + \mathbf{C}\dot{x} + \mathbf{K}x = F \tag{17}$$

$$\mathbf{M}\boldsymbol{\Psi}\ddot{\alpha} + \mathbf{C}\boldsymbol{\Psi}\dot{\alpha} + \mathbf{K}\boldsymbol{\Psi}\alpha = F \tag{18}$$

where $\boldsymbol{\Psi}$: Mode shape matrix, α : Modal coordinate vector, $\mathrm{x} = \boldsymbol{\Psi}\alpha$.

To use the orthogonality of the modes, both sides were multiplied by $\boldsymbol{\Psi}^T$ and rearranged to give [16-19]

$$\hat{\mathbf{M}}\ddot{\alpha} + \hat{\mathbf{C}}\dot{\alpha} + \hat{\mathbf{K}}\alpha = \hat{F} \tag{19}$$

where

$\hat{\mathbf{M}} = \boldsymbol{\Psi}^T\mathbf{M}\boldsymbol{\Psi}$, $\hat{\mathbf{C}} = \boldsymbol{\Psi}^T\mathbf{C}\boldsymbol{\Psi}$, $\hat{\mathbf{K}} = \boldsymbol{\Psi}^T\mathbf{K}\boldsymbol{\Psi}$, $\hat{F} = \boldsymbol{\Psi}^T F$.

The equation of motion expressed by Eq. (19) was transformed into the first-order mode function in Eq. (20). The calculated output $\bar{w}$ is a displacement vector, whose derivatives represent velocity and acceleration. $\hat{\mathbf{M}}$, $\hat{\mathbf{C}}$ and $\hat{\mathbf{K}}$ are the modal mass, modal damping, and modal stiffness, respectively. The damping value is defined to be proportional damping [20]. To use Eq. (20), a modal analysis was performed using ANSYS.

$$\begin{aligned}\dot{\alpha} &= \mathbf{A}_g\alpha + \mathbf{B}_g\hat{F} \\ \bar{w} &= \mathbf{C}_g\alpha + \mathbf{D}_g\hat{F}\end{aligned} \tag{20}$$

where

$$\mathbf{A}_g = \begin{bmatrix} 0 & 1 \\ -(\hat{\mathbf{M}})^{-1}\hat{\mathbf{K}} & -(\hat{\mathbf{M}})^{-1}\hat{\mathbf{C}} \end{bmatrix},\ \mathbf{B}_g = \begin{bmatrix} 0 \\ \hat{\mathbf{M}}^{-1} \end{bmatrix},$$

$$\mathbf{C}_g = \begin{bmatrix} 1 & 0 \\ 0 & 1 \\ -(\hat{\mathbf{M}})^{-1}\hat{\mathbf{K}} & -(\hat{\mathbf{M}})^{-1}\hat{\mathbf{C}} \end{bmatrix},\ \mathbf{D}_g = \begin{bmatrix} 0 \\ 0 \\ \hat{\mathbf{M}}^{-1} \end{bmatrix},\ \bar{w} = \begin{bmatrix} \alpha & \dot{\alpha} & \ddot{\alpha} \end{bmatrix}^T.$$

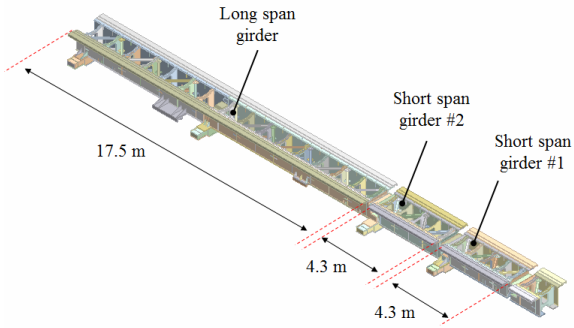

(a) Length of each segmented switch

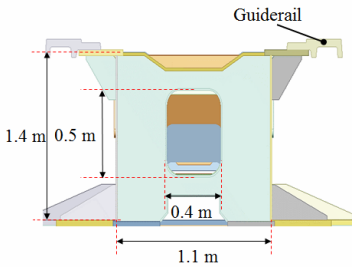

(b) Cross section

Fig. 9. Configuration of segmented switch and cross section.

The segmented switch for a Maglev vehicle is composed of three segments (Fig. 9) which are denoted as short span girder #1, short span girder #2, and long span girder. The short span girder is 4.2 m long, while the long span girder is 17.5 m long. The cross-sectional area of the short and long girders are 1.1 m and 1.4 m, respectively. The girders are made of steel.

Table 5 lists the modal parameters for each segment obtained by the mode analysis. The participation factor is the ratio of the modal mass to the entire mass, based on which the mode was selected [21].

For short span girder #1, the first and second vertical vibration modes were 81.1 Hz and 86.1 Hz, respectively, with participation factors of 82.7 % and 0.7 %, respectively. The participation factor is extremely low in the second vertical vibration mode compared to the first vertical vibration mode. A similar result was obtained in the vertical and lateral vibration modes of short span girder #2, which has a similar structure.

For the long span girder, the first and second vertical vibration modes were 12.95 Hz and 72.9 Hz, respectively, with participation factors of 67.5 % and 7.5 %, respectively. The participation factor in the second vertical vibration mode was higher and thus cannot be ignored. Most of the remaining modes were generated locally and were therefore not selected. The participation in the first and second lateral vibration modes were 67 % and 7.7 %, respectively.

Based on the results presented in Table 5, the first vertical mode and the first lateral mode were selected as the major modes in short span girders #1 and #2. The first and second vertical modes and the first and second lateral modes were selected as the major modes in the long span girder.

Table 5. Results of modal analysis of each segment.

		Short span girder #1	Short span girder #2	Long span girder
1st vertical vibration mode	Natural frequency	81.1 (Hz)	98.0 (Hz)	12.9 (Hz)
	Modal mass	5379.9 (kg)	3893.5 (kg)	20066.6 (kg)
	Participation factor	82.7 (%)	62.3 (%)	67.5 (%)
2nd vertical vibration mode	Natural frequency	86.1 (Hz)	129.9 (Hz)	72.9 (Hz)
	Modal mass	43.8 (kg)	12.4 (kg)	2157.6 (kg)
	Participation factor	0.7 (%)	1.8 (%)	7.5 (%)
1st lateral vibration mode	Natural frequency	48.7 (Hz)	58.2 (Hz)	10.1 (Hz)
	Modal mass	4187.9 (kg)	3811.3 (kg)	19613.8 (kg)
	Participation factor	63.8 (%)	58.1 (%)	66.2 (%)
2nd lateral vibration mode	Natural frequency	67.7 (Hz)	79.6 (Hz)	39.4 (Hz)
	Modal mass	65.4 (kg)	61.2 (kg)	2184.8 (kg)
	Participation factor	1 (%)	0.9 (%)	7.7 (%)

Table 6. Modal parameters of the segmented switch.

		Short span girder #1	Short span girder #2	Long span girder
Vertical vibration mode 1st / 2nd	Modal mass (kg)	5.4×10^3	3.9×10^3	2.0×10^4 / 2.2×10^3
	Modal stiffness (N/m)	1.4×10^9	1.5×10^9	1.3×10^8 / 4.5×10^8
	Modal damping (N/m/s)	1.1×105	9.6×10^4	6.5×10^4 / 4.0×10^4
Lateral vibration mode 1st / 2nd	Modal mass (kg)	4.2×10^3	3.8×10^3	2.0×10^4 / 2.2×10^3
	Modal stiffness (N/m)	3.9×10^8	5.1×10^8	7.9×10^7 / 1.3×10^9
	Modal damping (N/m/s)	5.1×10^4	5.6×10^4	4.9×10^4 / 2.2×10^5

Through the ANSYS analysis, the important vertical and lateral vibration modes for each segment were selected. The parameters needed for Eq. (18) were identified and are listed in Table 6. The axial vibration mode was not considered since the frequency appeared to be very high.

To express the determined mode shape $\boldsymbol{\Psi}$, the results of the modal analysis of each segment using ANSYS are shown in Fig. 11. The displacement in the vertical and lateral directions at each node were obtained and the normalized mode shape was created. Only the neutral axis and the vertical and lateral displacements of the girder were considered in the three dimensional mode shape, which was defined in two dimensions as shown in Fig. 10(b).

Using the same methodology, the mode shapes of three segments were superposed as shown in Fig. 11. The components of the final mode shape matrix $\boldsymbol{\Psi}$ expressed in Eq. (19) are defined in Eq. (21). Each mode shape was placed at 0.1 m intervals over the 50 m-long axial direction. Therefore,

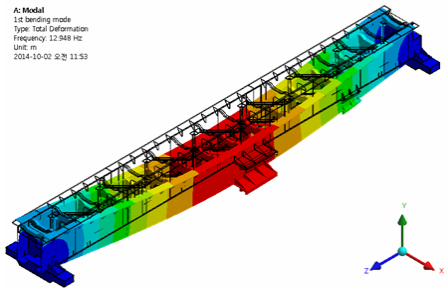

(a) Results of modal analysis

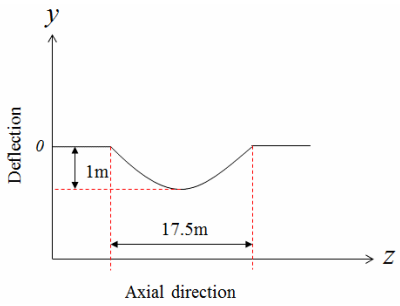

(b) Normalization of mode shape

Fig. 10. Definition of mode shape.

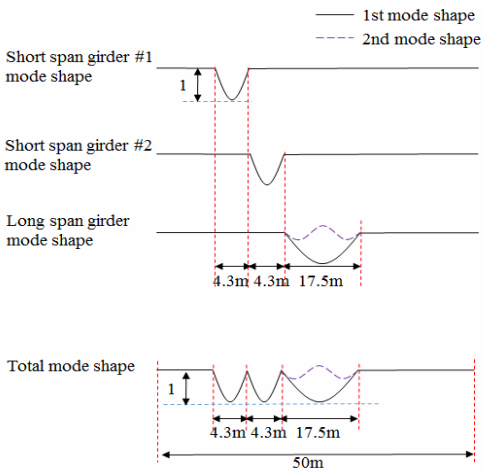

Fig. 11. Mode shape for segmented switch.

the size of the matrix in Eq. (21) is 501 × 8.

$$\boldsymbol{\Psi} = \left[\boldsymbol{\Psi}^{S\#1}_{1stver}, \ \boldsymbol{\Psi}^{S\#2}_{1stver}, \ \boldsymbol{\Psi}^{L}_{1stver}, \ \boldsymbol{\Psi}^{L}_{2ndver}, \ \boldsymbol{\Psi}^{S\#1}_{1stlat}, \ \boldsymbol{\Psi}^{S\#2}_{1stlat}, \ \boldsymbol{\Psi}^{L}_{1stlat}, \ \boldsymbol{\Psi}^{L}_{2ndlat} \right]^{T}_{501X8} \tag{21}$$

where *S*#1 : Short span girder #1, *S*#2 : Short span girder #2, *L* : Long span girder #1, 1*stver* : 1st vertical direction, 1*stlat* : 1st lateral direction, 2*ndver* : 2nd vertical direction, 2*ndlat* : 2nd lateral direction.

2.5 Analysis process

In Sec. 2.1, the multibody dynamics of the Maglev vehicle

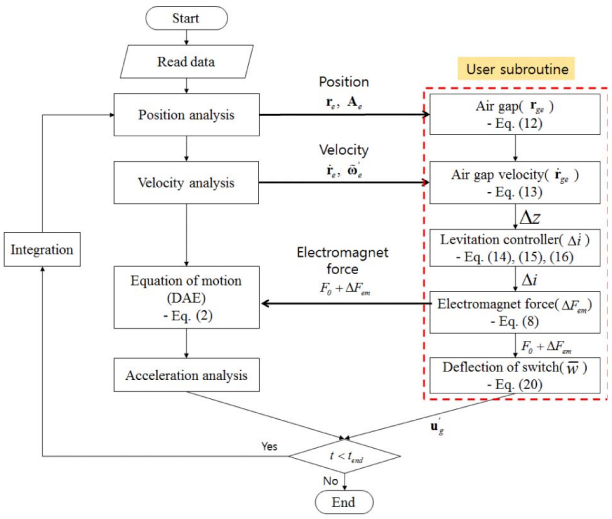

Fig. 12. Flow chart of the integrated model with Maglev vehicle and segmented switch.

and the bogie system were modeled using Virtual Lab Motion [22]. The electromagnet model, the levitation electromagnet controller, and the segmented switch described in Secs. 2.2-2.4 were implemented as subroutines.

Fig. 12 presents the flow chart of the integration model. The position and the velocity of each body is modeled and the airgap and airgap velocity are calculated using the orientation matrix. The position and velocity vectors of the electromagnet are also calculated. The controlling electrical current is estimated through the electromagnet controller using the calculated airgap. The electromagnet force is calculated using the controlled electric current and the airgap, each of which is fed into the equation of motion and the segmented switch module. The deflection of each segment is calculated in the segmented switch module. Eqs. (12) and (13) were transformed into the coordinates of the deformation to give Eqs. (22) and (23).

$$\mathbf{r}_{ge} = \mathbf{r}_g + \mathbf{A}_g(\mathbf{s}'_{ge} + \mathbf{u}'_g) - (\mathbf{r}_e + \mathbf{A}_e\mathbf{s}'_{eg}) \tag{22}$$

$$\dot{\mathbf{r}}_{ge} = \dot{\mathbf{r}}_g + \mathbf{A}_g\tilde{\boldsymbol{\omega}}'_g(\mathbf{s}'_{ge} + \mathbf{u}'_g) + \mathbf{A}_g\dot{\mathbf{u}}'_g - (\dot{\mathbf{r}}_e + \mathbf{A}_e\tilde{\boldsymbol{\omega}}'_e\mathbf{s}'_{eg}) \tag{23}$$

where

$$\mathbf{u}'_g = \boldsymbol{\Phi}\alpha, \quad \mathbf{u}'_g = \begin{bmatrix} 0 & \Delta v & \Delta w \end{bmatrix}^T, \quad \dot{\mathbf{u}}'_g = \begin{bmatrix} 0 & \dot{v} & \dot{w} \end{bmatrix}^T.$$

3. Stability simulation of a Maglev vehicle over a segmented switch

In this section, the vibrations and vehicle traversal were analyzed based on multibody dynamics using the integration model of the segmented switch with the Maglev vehicle system. The aim was to evaluate levitation stability in terms of the vibration of the segmented switch, and the operational safety upon contact when the vehicle passes over a curve of the segmented switch. For each of the two cases, the simulation conditions were imposed as listed in Table 7. The levitation stability was evaluated by analyzing the levitation airgap when the Maglev vehicle stopped on the switch [23]. The operational safety was evaluated according to the velocity of the vehicle by analyzing the lateral airgap when the vehicle traveled at a constant speed starting 5 km/h with a regular increase of 5 km/h after a specified time interval.

Table 7. Simulation conditions.

	Case 1	Case 2
Purpose	Evaluation of levitation stability	Evaluation of operational safety
Assumption	Resonance with the segmented switch	Traveling over a segmented switch
Vehicle speed	Standstill (0 km/h)	5–25 km/h
Results of interest	Vertical airgap history	Lateral airgap history

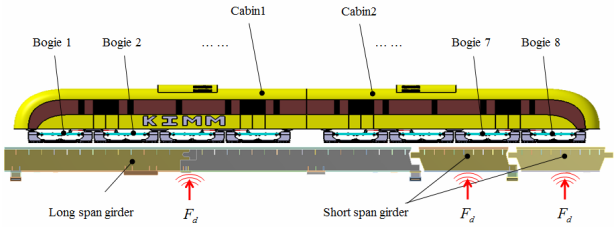

Fig. 13. Imposing a force on the center of each segment of the switch.

3.1 Vibration simulation of the Maglev vehicle during resonance with the segmented switch

To assess the levitation stability in terms of the airgap, vibrations were generated at the segmented switch. As shown in Fig. 13, when the Maglev vehicle is stationary on the segmented switch, a force was imposed on the center of each segment of the switch to cause forced vibrations. The force increased over time as described in Eq. (24) to induce a forced vibration from 0 up to high frequency.

$$F_d = 10^4 \sin(\mathrm{wt}\times \mathrm{t}) . \tag{24}$$

The input force caused a resonance vibration in the vertical and lateral directions in each segment of the switch, as shown in Fig. 14. Table 8 lists the displacements of the resonance vibration measured at the center of each segment of the switch. There was an initial displacement due to the vertical deflection caused by the weight of the vehicle.

The vertical deflection oscillations were between -0.6 mm to 0.4 mm in short span girder #1 and between -0.4 mm to 0.2 mm in short span girder #2. Approximately -1.7 mm of the long span girder was deflected, based on which approximately ±2.2 mm and ±1.1 mm of deflection were measured for the first and second resonance, respectively.

The lateral deflection oscillations occurred in the ranges of approximately ±1.3 mm and ±1.1 mm of for short span girder #1 and #2, respectively. In the long span girder, the first and

Table 8. Deflection of each segmented switch.

	Modes	Deflection	Fluctuation amplitude
Short span girder #1	1st vertical mode	-0.1 mm	0.4 mm ~ -0.6 mm
	1st lateral mode	-0 mm	1.3 mm ~ -1.3 mm
Short span girder #2	1st vertical mode	0.1 mm	0.2 mm ~ -0.4 mm
	1st lateral mode	0 mm	1.1 mm ~ -1.1 mm
Long span girder	1st vertical mode	-1.7 mm	0.4 mm ~ -3.9 mm
	2nd vertical mode	-1.7 mm	-0.5 mm ~ -2.8 mm
	1st lateral mode	0 mm	3.5 mm ~ -3.5 mm
	2nd lateral mode	0 mm	3.7 mm ~ -3.7 mm

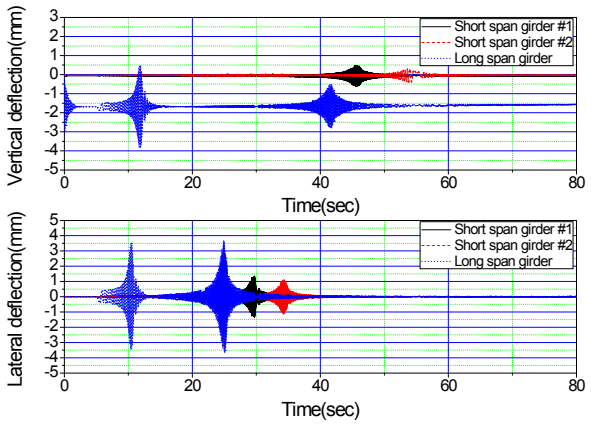

Fig. 14. Validation of the resonance vibration of each segment.

second vibrations were in the amplitude ranges of ±3.5 mm and ±3.7 mm, respectively. The longer the girder, the greater the vibration. The impact of the vibration was greater in the lateral than the vertical direction.

When resonance occurred in each segment, the time histories of the vertical and the lateral airgaps between the segmented switch and the magnet of each bogie of the Maglev vehicle are shown in Fig. 15. The vertical airgap oscillated in the range ±1.2 mm and ±0.7 mm in bogies 1 through 6 by the first and second modes of the long span girder on the basis of 8 mm. Currently, 8 mm is the target vertical airgap distance that serves as the standard for levitation control. From Table 8, when resonance occurred in the long span girder of the segmented switch, the changes in displacement were approximately ±2.3 mm in the first mode and ±1.7 mm in the second mode, which were reduced to less than 50 % of the amplitude by the levitation controller. Bogies 7 and 8 were located on the short span girder and experienced displacements of approximately ±0.1 mm. This was less than approximately 10 %–20 % compared to the vibrations generated by resonance over a vertical airgap of 8 mm.

Fig. 16 shows the time histories of the lateral airgaps. The changes in the lateral airgap were the greatest in bogie 3, which was positioned on the center of the long span girder. The oscillations occurred within a range over ± 4 mm. This implies that the deflection of the long span girder caused by

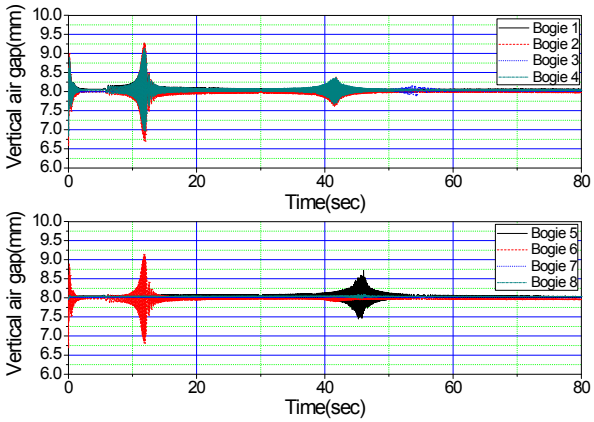

Fig. 15. Time histories of the vertical airgap.

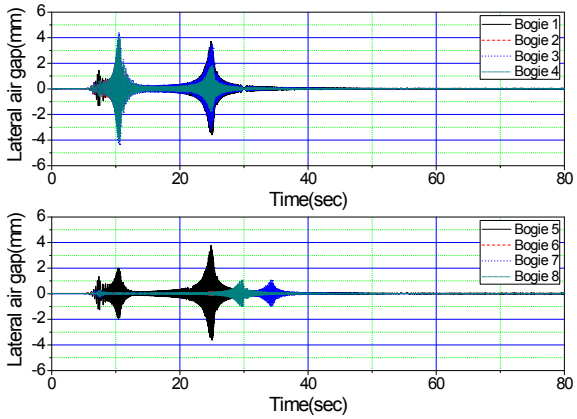

Fig. 16. Time histories of the lateral airgap.

the first vibration mode did not change and was reflected onto the lateral airgap. Likewise, when the rest of the lateral airgaps were compared, the scale of vibration of a segment was also reflected as it stands. Therefore, the vibration of the structure had a constant influence on the vehicle when the vibration of the structure was not controlled as it traveled on a curved rail. Therefore, it is necessary to check whether contact occurred by analyzing the changes in the lateral airgap relative to the velocity of the vehicle based on an analysis of the vehicle's travel characteristics on the curved rail.

3.2 Simulations of the Maglev vehicle traveling over a segmented switch

Real tests were performed to determine whether contact was made between the vehicle and a switch to ensure passenger safety when the vehicle runs over a switch. The velocity was increased from 5 km/h to 25 km/h in intervals of 5 km/h. Contact was determined by focusing on the changes in the lateral airgap between the switch and the vehicle. As a point reference, if the geometric structure exceeds 13.5 mm, there is the possibility of contact occurring.

Fig. 17 shows the changes in the lateral airgap for different

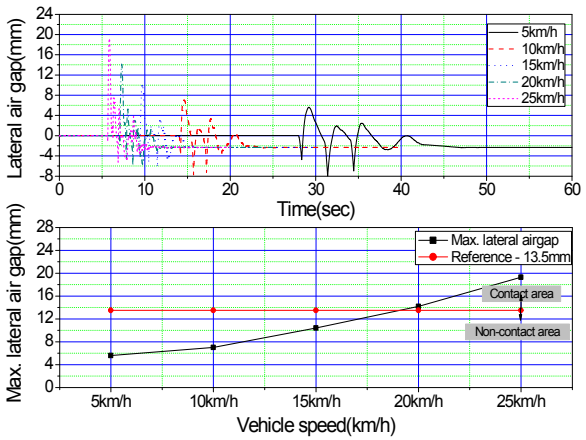

Fig. 17. Lateral airgap simulation results.

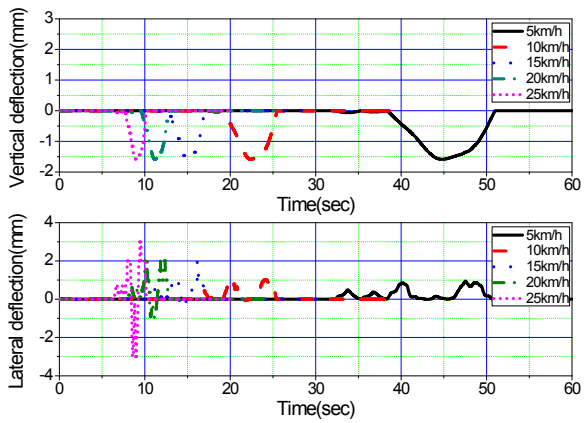

Fig. 18. Vertical and lateral vibration response of segmented switch.

vehicle velocities on the left and the maximum displacement on the right. The front part of the bogie that first enters the curve was used to obtain the greatest lateral airgap. From the analytical results, the lateral airgap fluctuated within 10 mm for velocities of 5–15 km/h. The lateral airgap was approximately 14 mm and 19 mm for velocities of 20 km/h and 25 km/h, respectively, which indicate the possibility of contact. The maximum lateral airgap increased linearly with the vehicle velocity (Fig. 16). As a result, contact is expected to be made at a velocity of approximately 18 km/h.

Fig. 18 illustrates the amplitude of vibrations generated in the vertical and lateral directions of the switch for different vehicle velocities. The vertical vibration of the switch was constant regardless of the vehicle velocity. In addition, the greater the velocity, the greater the lateral vibration of the switch. This implies that the centrifugal force is related to the restoring force of the electromagnet.

The lateral deflection of the switch was a maximum of approximately 6 mm at a velocity of 25 km/h. From Fig. 17, vibrations with an amplitude of approximately 6 mm occurred at the same velocity. Therefore, the centrifugal force created by the vehicle velocity was greater than the restoring force of

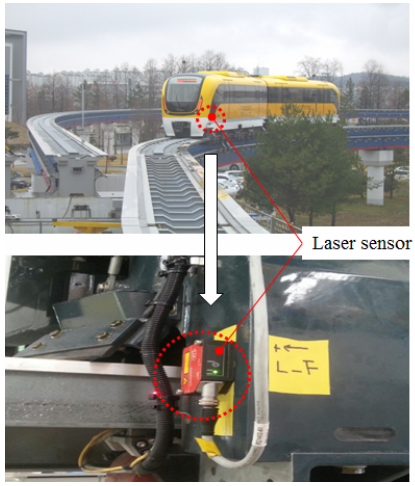

Fig. 19. Sensor locations for measurement of lateral airgaps.

the electromagnet. The exception was when structural vibrations were generated by the contact between the Maglev vehicle and the switch. Using this analytical method, a travel velocity that is suitable for avoiding contact can be identified.

3.3 Experimental test of the Maglev vehicle over a curved segmented switch

Experiment was carried out to verify the coupled dynamics model between the Maglev vehicle and the segmented switch. We measured the lateral airgaps when the Maglev vehicle traveled over the curved segmented switch at speeds of 5 km/h to 25 km/h. Laser sensors were employed to measure the distance between side frame of the bogie and the side of the rails as shown in Fig. 19. They were located the foremost bogie in the travel direction to record the largest lateral displacement.

The lateral airgap was measured at vehicle speeds of 5, 15 and 25 km/h. The maximum lateral airgaps were approximately 6.4 mm, 9.8 mm, 18.6 mm at each speed (Fig. 20). This is similar to the simulation results shown in Fig. 17. It is also the similar that contact between the side frames of bogie and the rail occurred at a vehicle speed of about 18 km/h. Therefore, the proposed coupled dynamic model will be helpful for the prediction of stability and safety in Maglev vehicles.

4. Conclusions

An analytical model was developed to verify the levitation stability and operational safety of a segmented switch for a Maglev vehicle developed in Korea. The cabin, bogie, and electromagnet parts of a Maglev vehicle were modeled based on multibody dynamics. The electromagnet was linearized and a model was developed for the levitation controller. The flexibility of the segmented switch was taken into account via vibration mode analysis. The dynamic model of the segmented switch was composed using the superposition method. The dynamic models developed in this study were integrated into the proposed analysis process.

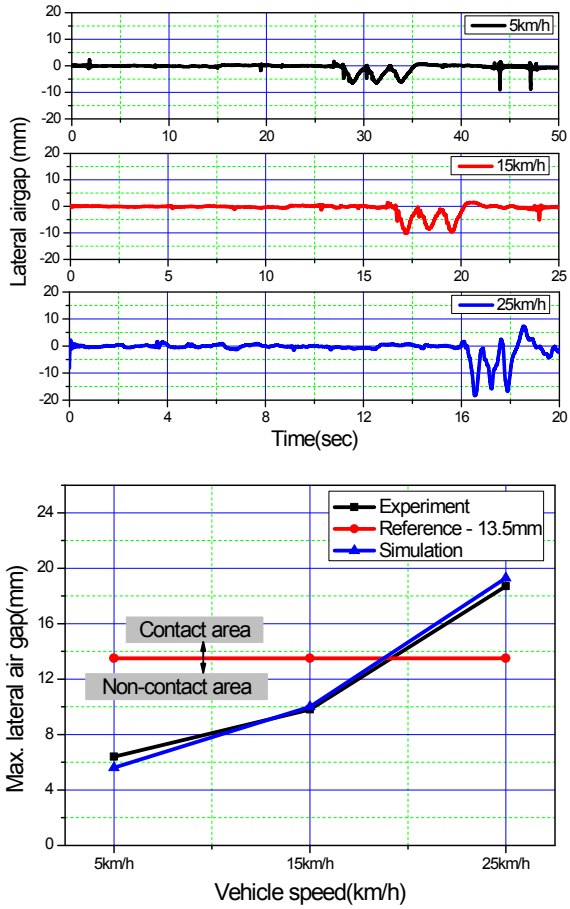

Fig. 20. Experimental results of lateral airgap.

When resonance occurred in the segmented switch, an analysis of the levitation stability of the Maglev vehicle was performed. When the Maglev vehicle was traveling over the segmented switch, the operational safety was analyzed for different velocities. The focus of each analysis was the vertical and lateral airgaps. The vibration amplitude was reduced by the levitation controller despite the occurrence of resonance. Contact can be made when the vehicle runs over the switch over a certain velocity threshold. The velocity at which no contact was made was calculated to be approximately 18 km/h. The current analysis model was verified via experimental measurements of the lateral airgap between a Maglev vehicle and the segmented switch.

The proposed analysis mode enables the assessment of the levitation stability and operational safety of the vehicle before deployment. Additionally, the model proposed in this study can be used to improve the levitation control algorithm.

Acknowledgments

This research was supported by a grant [16RTRP-B070544-04] from Railroad Technology Research Program funded by Ministry of Land, Infrastructure and Transport of Korean government.

References

[1] H. S. Han, B. H. Yim, N. J. Lee, Y. J. Kim and B. H. Kim, Prediction of ride quality of a Maglev vehicle using a full vehicle multi-body dynamic model, *Vehicle System Dynamics*, 47 (10) (2008) 1271-1286.

[2] H. S. Han, A study on the dynamic modeling of a magnetic levitation vehicle, *JSME International*, 46 (4) (2003) 1497-1501.

[3] B. H. Yim, H. S. Han, J. K. Lee and S. S. Kim, Curving performance simulation of an EMS-type Maglev vehicle, *Vehicle System Dynamics*, 47 (10) (2009) 1287-1304.

[4] H. S. Han, B. H. Yim, J. K. Lee, Y. C. Hur and S. S. Kim, Effects of Guideway's vibration characteristics on the dynamics of a Maglev vehicle, *Vehicle System Dynamics*, 47 (3) (2009) 309-234.

[5] H. S. Han, J. M. Lee, B. H. Kim, H. K. Sung and K. J. Kim, Dynamic modelling of a magnetically levitated vehicle running over a flexible guideway, *Proceedings of the ECCOMAS 2007* (2007).

[6] B. H. Yim and H. S. Han, Curve negotiation analysis of a Maglev vehicle utilizing electromagnetic suspension system, *Proceedings of the Asian Conference on Multibody Dynamics 2008* (2008).

[7] K. Fichtner and F. Pichlmeier, The Transrapid guideway switch test and verification, *Proceedings of the MAGLEV 2004* (2004).

[8] F. Dignath, X. F. Liu and Q. H. Zheng, Dynamic behavior of guideway switch beams, *Proceedings of the MAGLEV 2006* (2006).

[9] J. M. Lee, H. J. Cho, K. S. Rho and D. S. Kim, Development of Maglev switch for the urban uransit Maglev in Korea, *Proceedings of the MAGLEV 2008* (2008).

[10] D. Zhou, C. Hansen, J. Li and W. Chang, Review of coupled vibration problems in EMS maglev vehicles, *International Institute of Acoustics and Vibration*, 15 (1) (2010) 10-23.

[11] *LMS virtual lab motion users manual*, LMS International.

[12] E. J. Haug, *Computer-aided kinematics and dynamics of mechanical system*, ALLYN AND BACON Pub, USA (1989).

[13] A. A. Shabana, *Railroad vehicle dynamics: A computational approach*, Taylor & Francis Group, USA (2007).

[14] P. K. Sinha, *Electromagnetic suspension dynamics & control*, Peter Peregrinus Ltd, London (1987).

[15] J. B. Han, J. K. Kim, J. M. Lee and H. S. Han, Analysis on dynamics characteristics of Maglev vehicle with considering a non-linear levitation force of electromagnet, *Proceedings of the KSME 2011* (2011).

[16] S. P. Jung and T. W. Park, Analysis and control of the flexible multibody system using MATLAB, *Transactions of the Korean Society of Mechanical Engineers*, 32 (5) (2008) 437-443.

[17] J. H. Lee, J. H. Sohn, K. S. Kim and W. S. Yoo, Compari-

son of large deformation of cantilever beam with computer simulation using modal coordinates, *Proceedings of KSME 2002* (2002).
[18] A. A. Shabana, Flexible multibody dynamics: Review of past and recent developments, *Multibody System Dynamics*, 1 (2) (1997) 189-222.
[19] A. A. Shabana, Computer implementation of the absolute nodal coordinate formulation for flexible multibody dynamics, *Multibody System Dynamics*, 16 (3) (1998) 293-306.
[20] Y. B. Yang, J. D. Yau and Y. S. Wu, *Vehicle-bridge interaction dynamics with application to high-speed railway*, World Scientific Pub, Singapore (2004).
[21] T. Irvine, *Effective modal mass & modal participation factors revision H* (2013).
[22] K. E. Atkinson, *An introduction to numerical analysis*, John Wiley & Sons Inc. (1978).
[23] E. Coenraad, *Modern railway track second edition*, C. Esveld, Netherlands (2001).

Jong-Boo Han received his B.S. degree in Mechatronics Engineering from Chungnam National University, Daejeon, Korea, in 2009. He received his M.S. degree in Mechatronics Engineering from Chungnam National University, in 2011. He is currently Ph.D. candidate of Mechatronics Engineering at Chungnam National University, Daejeon, Korea.

Hyung-Suk Han received the Ph.D. degree in mechanical engineering from Ajou University, Suwon, Korea, in 1997. Since 1997, he has been a Principal Researcher in KIMM (Korea Institute of Machinery and Materials). His research interest is the dynamic simulation of maglev vehicles.

Jong-Min Lee received his B.S. degree in Mechanical Design Engineering from Chungnam National University, Daejeon, Korea, in 1991. He received his M.S. degree in Mechanical Design Engi-neering from Chungnam National University, Daejeon, Korea, in 1993. He received his Ph.D. degree in Mechanical Design Engineering from Chungnam National University, Daejeon, Korea, in 2011.

Sung-Soo Kim received his B.S. degree in Agricultural Engineering from Seoul National University, Seoul, Korea, in 1981. He received his M.S. degree in Mechanical Engineering from University of Iowa, Iowa city, Iowa, U.S.A., in 1983, and his Ph.D. degree in Mechanical Engineering from University of Iowa, Iowa city, Iowa, U.S.A., in 1988. He is currently a Professor of Mechatronics Engineering at Chungnam National University, Daejeon, Korea.